A 3-D Force and Moment Motor for Small-Scale Biomechanics Experiments

Sim, J H ; Puria, S

Abstract: The inability to identify 3-D force and moment components for actuators and sensors is a major limiting factor in the study of 3-D force interactions with small-scale biological structures. While recent advances have been made in the measurement of stimulating forces using load cells and atomic-force microscopy in experimental preparations of biological structures such as mammalian temporal bones, these techniques have mostly been limited to one or two dimensions. In this paper, a method is described for stimulating biological structures using a small magnet (2 mg Sm2Co17) and a nearby current-conducting coil (46 gauge, 50 turns), that allows the 3-D Lorentz forces and moments acting on the magnet to be calculated. To make these calculations possible, the dimensions and placements of the magnet and coil are accurately determined (within 10 mum for in vitro preparations) using high-resolution micro-CT imaging. This noncontact force motor method has been used to study the mechanics of the malleus-incus complex in the mammalian middle ear in addition to basilar membrane mechanics and fluid flow inside the cochlea, and it can also be applied to the study of other biomechanical structures.

DOI: https://doi.org/10.1109/JSEN.2009.2030879

A 3-D Force and Moment Motor for Small-Scale Biomechanics Experiments

Jae Hoon Sim and Sunil Puria

***Abstract*—The inability to identify 3-D force and moment components for actuators and sensors is a major limiting factor in the study of 3-D force interactions with small-scale biological structures. While recent advances have been made in the measurement of stimulating forces using load cells and atomic-force microscopy in experimental preparations of biological structures such as mammalian temporal bones, these techniques have mostly been limited to one or two dimensions. In this paper, a method is described for stimulating biological structures using a small magnet (2 mg Sm_2Co_{17}) and a nearby current-conducting coil (46 gauge, 50 turns), that allows the 3-D Lorentz forces and moments acting on the magnet to be calculated. To make these calculations possible, the dimensions and placements of the magnet and coil are accurately determined (within 10 μm for *in vitro* preparations) using high-resolution micro-CT imaging. This noncontact force motor method has been used to study the mechanics of the malleus-incus complex in the mammalian middle ear in addition to basilar membrane mechanics and fluid flow inside the cochlea, and it can also be applied to the study of other biomechanical structures.**

***Index Terms*—Cochlea, coil, electromagnetic, force, magnet, micro-computed tomography (micro-CT), middle ear, moment.**

I. Introduction

THE STUDY of the interactions between three-dimensional (3-D) forces and small-scale biological structures has been limited by the techniques available for measuring *in situ* excitation forces. Such excitation forces are typically measured in only one dimension using load cells, though there have also been efforts to measure them in two dimensions using atomic force microscopy techniques [1]. Piezoelectric micro-actuators represent another technique for exciting biological structures with calculated or calibrated forces [2]–[4], but for such actuators the 3-D force and moment components are nearly impossible to measure. As the dimensions of a given biological structure of interest become smaller, the measurement of excitation forces becomes increasingly difficult, and even estimations of the forces can suffer from relatively large errors due to inaccuracies in determining the dimensions and positions of the actuator and structures under study. In this paper, a method is described for exciting biological structures using a small magnet and a current-conducting coil, for which the 3-D Lorentz forces and moments are calculated after extracting accurate measurements of the shapes and relative positions of the magnet and coil from micro-CT images. In addition to its capability of predicting 3-D force and moment components, this method provides a safer way to stimulate delicate biological structures, since only the small magnet is attached to the biological structure and the stimulating forces are transferred without any contact with the coil apparatus. The 3-D force and moment components with this method can be adjusted by changing the relative positions and orientations of the magnet and coil.

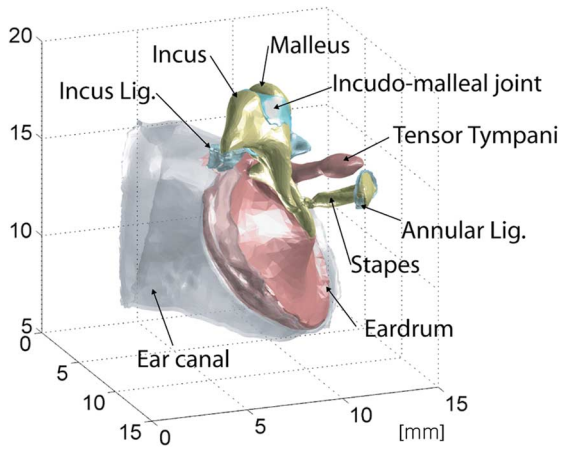

Fig. 1. Middle-ear structures of a human ear. The three middle-ear bones (the malleus, incus, and stapes) form an ossilcular linkage between the ear drum and the cochlea, suspended by ligaments and tendons in the middle-ear cavity.

In this study, stimulation with a magnet-coil drive system is applied to two experimental setups of the human middle ear, in which the tympanic membrane (TM) has been removed. The middle-ear in mammals is distinguished from the middle ears of other vertebrates by the presence of three distinct bones forming the linkage between the ear drum and the cochlea [5], [6]. These bones (the malleus, incus, and stapes) are suspended by ligaments and tendons in the middle-ear cavity, and are believed to help endow mammals with their unique capacity for high-frequency hearing [5], [7], [8]. Fig. 1 shows the middle-ear structures of a human ear. In the experimental setup of Ear 1, which aims to characterize the dynamics of the isolated malleus-incus complex, the malleus is stimulated by the magnet-coil drive system. In the experimental setup of Ear 2, which is designed to characterize the incudo-malleal joint (IMJ) between the malleus

Manuscript received March 25, 2009; revised July 06, 2009; accepted August 12, 2009. Current version published October 28, 2009. This work was supported in part by a grant from the National Institute of Deafness and Communication Disorders (NIDCD) of the NIH (DC005960). The associate editor coordinating the review of this paper and approving it for publication was Prof. Okyay Kaynak.

J. H. Sim was with Stanford University, Stanford, CA 94305 USA. He is now with the Department of ORL-Clinic, University Hospital Zurich, 8091 Zurich, Switzerland (e-mail: JaeHoon.Sim@usz.ch).

S. Puria is with the Department of Mechanical Engineering and the Department of Otolaryngology-Head and Neck Surgery, Stanford University, Stanford, CA 94305 USA (e-mail: puria@stanford.edu).

Color versions of one or more of the figures in this paper are available online at http://ieeexplore.ieee.org.

Digital Object Identifier 10.1109/JSEN.2009.2030879

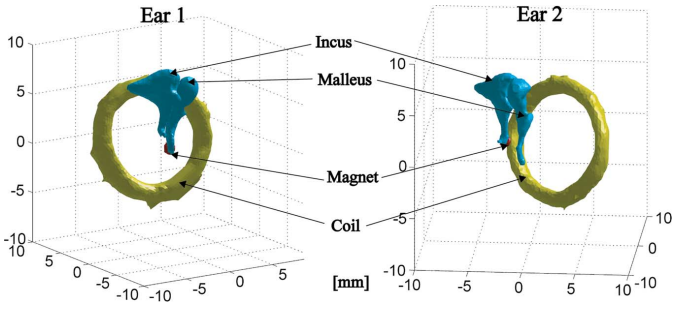

Fig. 2. The magnet and coil force motor, as used in a middle-ear experiment. The stapes and the TM were removed in order to isolate the malleus-incus complex. A 2.0 mg Sm_2Co_{17} magnet (1.13 ± 0.03 Tesla) was attached to the umbo for Ear 1 (left), while it was attached to the tip of the long crus of the incus for Ear 2 (right). The coil (consisting of 50 turns of 46 gauge wire), was mounted around the bony annulus of the TM (not shown) using dental cement.

and the incus, the incus is stimulated by the magnet-coil drive system (Fig. 2).

With the middle-ear structures stimulated by electromagnetic force between the magnet and the coil, 3-D motions of the malleus and the incus in both experimental setups are measured using a Laser Doppler Vibrometer (LDV) [9], [10]. The applied electromagnetic force is calculated using the dimensions and relative positions of the magnet and the coil, as determined from micro-CT images, and the work rate exerted by the electromagnetic force is calculated to represent the interaction between the stimulation and the structure.

II. Methods

A. Temporal Bone Preparation

Two human cadaver temporal bone preparations were used for this study. In both preparations, the stapes and the TM were removed so that the dynamics of the malleus-incus complex could be observed in isolation. The entire medial parts of the temporal bones were also removed to allow access by the laser beam from the LDV system.

In the experimental setup of Ear 1, a 2.0-mg Sm_2Co_{17} magnet (1.13 ± 0.03 Tesla) of a thin frustrum shape was attached to the umbo (the lateral side of the tip of the long process of the malleus), and the coil bundle (50 turns of 46 gauge wire) was mounted around the bony annulus of the TM using dental cement.

In the experimental setup of Ear 2, the malleus was fixed to the peripheral middle-ear cavity bone using dental cement, and ligaments attached to the incus were removed so that the incus was suspended only by the IMJ. The same magnet was attached to the tip of the long process of the incus (on the lateral side, opposite the Lenticular process that connects to the head of the stapes). The same coil bundle was also mounted around the bony annulus of the TM. The magnet and the coil bundle in Ear 1 and Ear 2 were oriented relative to the malleus-incus complex in the manner shown in Fig. 2.

Five retro-reflective beads of 50 micron diameter were attached to the malleus (Ear 1) or the incus (Ear 2) as targets for the laser beam from the LDV system. The beads were glued on the medial side of the malleus or incus, and were held in position during the micro-CT scan and velocity measurements.

B. Micro-CT Imaging

The Lorenz force exerted on a magnet by a current-carrying coil depends on the shape and dimensions of the magnet and coil, along with their relative positions and orientations. All of these pieces of information can be extracted from high-resolution micro-CT scans. In this study, the *vivaCT 40* micro-CT scanner (*SCANCO Medical AG*) was used. In performing scans with metallic materials such as the coil and magnet, the energy level of the photons in the X-ray beam must be selected such that the images are clear and metal artifacts are minimized [11], [12]. The metal artifacts were minimized by setting the photon energy level to 70 keV, which is the maximum value allowed by the *vivaCT 40* micro-CT scanner.

The resulting grayscale values of the magnet and coil were above 980 for the scanner and scan conditions of this study, in which the maximum value of 1000 corresponds to an X-ray attenuation value of 8 cm^2/g [13], [14]. These values were easily distinguishable from bone, which typically has values below 550. The 3-D volumes of the magnet and coil were reconstructed from stacks of micro-CT slice images, as shown in Fig. 3(a). The 3-D geometry of the coil was then approximated as a torus with a rectangular cross section, as shown in Fig. 3(b), and the magnet was approximated as a frustum (i.e. a cone with the top cut off parallel to the base), as shown in Fig. 3(c). These simplified shapes closely approximate the actual geometries of the coil and magnet.

The X, Y, and Z axes form the coordinate frame for the coil, in which the coil rests on the XY plane and the Z axis passes through the center of the coil [Fig. 3(b)]. The x, y, and z axes, in turn, form the coordinate frame for the magnet, in which an untilted magnet would rest on the xy plane (parallel to the XY plane), and the z axis passes through the central axis of the untilted magnet [Fig. 3(c)]. The relative positions of the magnet and coil are described by the vector $\mathrm{r}_{\mathrm{off}}$, which extends from the origin of the coil coordinate frame ($X = 0$, $Y = 0$, and $Z = 0$) to the origin of the magnet coordinate frame ($x = 0$, $y = 0$, and $z = 0$). The origin of the magnet coordinate frame has coordinates of $X = X_{\mathrm{off}}$, $Y = Y_{\mathrm{off}}$, and $Z = Z_{\mathrm{off}}$ in the coil coordinate frame. The orientation of the magnet is described in terms of the tilt angle α, by which the untilted magnet is rotated about the y axis, as well as the tilt angle β, by which the α-tilted magnet is subsequently rotated about the z axis [Fig. 3(d)].

C. Force and Moment Calculations

To describe the magnetic field produced by a permanent magnet, the magnet can be represented as a solenoid that produces approximately the same magnetic field [15], [16]. The magnetization vector of the permanent magnet, $\mathbf{M}$, can be described in terms of the magnetic field vector, $\mathbf{B}$, the magnetic field intensity vector, $\mathbf{H}$, and the magnetic permeability of free space μ_0:

$$\mathbf{M} = \frac{\mathbf{B}}{\mu_0} - \mathbf{H}. \tag{1}$$

The magnetization vector, along with the unit normal vector to the magnet surface, $\mathbf{n}$, can then be used to calculate an equiv-

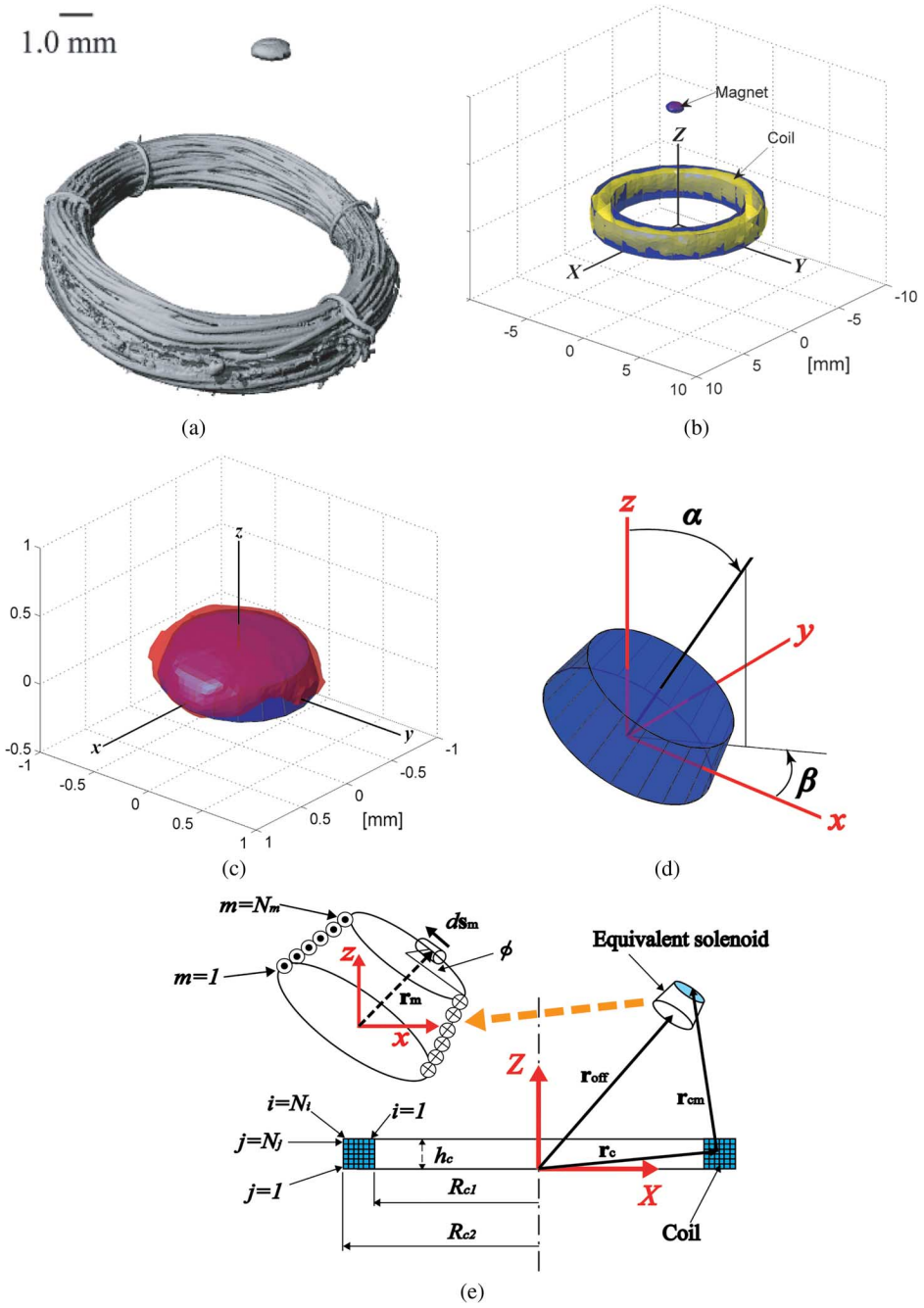

Fig. 3. Depictions of the magnet and coil force motor. (a) 3-D volume reconstruction of the coil and magnet based on micro-CT images, (b) approximation of the coil (yellow) as a torus with rectangular cross-section (blue) in the coil coordinate frame, with the magnet also shown, (c) approximation of the magnet (red) as a frustum (blue) in the magnet coordinate frame, (d) representation of the magnet orientation in terms of tilt angles α and β, and (e) representation of the coil and equivalent solenoid geometries as used for the calculations of the magnetic field, forces, and moments.

alent surface magnetization current density per unit height of the permanent magnet, $\mathbf{J_{sm}}$:

$$\mathbf{J_{sm}} = \mathbf{M} \times \mathbf{n}. \tag{2}$$

This, along with the height of the permanent magnet, h_m, can then be used to find the current in the equivalent solenoid, $I_{\rm eq}$, with N_m turns:

$$I_{eq} = |\mathbf{J_{sm}}| \frac{h_m}{N_m}. \tag{3}$$

The volume magnetization current density was neglected under the assumption that the magnetization is uniform throughout the volume of the magnet.

Next, the Biot–Savart law was used to compute the magnetic field, as produced by the coil, at each point in space within the turns of the equivalent solenoid [Fig. 3(e)]. The vector r_c indicates the position vector of a coil element, which is denoted by the row (i) and column (j) of the particular wire being pointed to, as well as by the angle θ of this point around the coil, from the origin of the coil frame ($X = 0$, $Y = 0$, $Z = 0$). The tip of this vector points to a vector ds_c, of infinitesimal length, that points

in the direction of current flow within the wire at that point. Similarly, within the equivalent solenoid, the vector r_m indicates the position vector of a solenoid element from the origin of the magnet frame ($x = 0$, $y = 0$, $z = 0$), within a specific "wire" (m) running around the outer surface of the solenoid, at an angle ϕ around the "wire." The vector of an infinitesimal length $d\mathbf{s}_m$, in turn, points in the direction of current flow within the "wire" at that point. The vector $\mathbf{r}_{cm}$, which points from $d\mathbf{s}_c$ to $d\mathbf{s}_m$, can then be defined as

$$\mathbf{r}_{cm} = \mathbf{r}_{\text{off}} + \mathbf{r}_m - \mathbf{r}_c. \tag{4}$$

The magnetic field, as produced by the coil, within the point (m, ϕ) of the equivalent solenoid, $\mathbf{B}(m, \phi)$, can then be calculated by integrating the Biot–Savart equation across all coil elements, with a coil current I_c:

$$\mathbf{B}(m,\phi) = \int_{i,j,\theta} d\mathbf{B}(i,j,\theta,m,\phi) = \int \frac{\mu_o}{4\pi} \frac{I_c d\mathbf{s}_c \times \mathbf{r}_{cm}}{|\mathbf{r}_{cm}|^3}. \tag{5}$$

Finally, the resultant forces, $\mathbf{F}$, and moments, $\boldsymbol{\tau}$, acting upon the origin of the magnet frame can be calculated from the Lorenz magnetic force equation, which is an alternative expression of Ampere's law of force:

$$\mathbf{F} = \sum_m \sum_\phi d\mathbf{F}(m,\phi) = \sum_m \sum_\phi \left(I_{\text{eq}} d\mathbf{s}_m(m,\phi) \times \mathbf{B}(m,\phi)\right) \tag{6}$$

and

$$\boldsymbol{\tau} = \sum_m \sum_\phi d\boldsymbol{\tau}(m,\phi) = \sum_m \sum_\phi \left(\mathbf{r}_m(m,\phi) \times d\mathbf{F}(m,\phi)\right). \tag{7}$$

For the actual numerical integrations, the angles θ and ϕ were divided into 100 discrete steps, N_i was set to 50 and N_j was set to 50 (in the coil), and N_m (in the equivalent solenoid) was also set to 50.

D. Force Measurement in One Dimension

In order to test the accuracy of the force and moment calculations, the force produced by a coil and magnet motor was both calculated and measured in one dimension using a load cell (*Entran ELG-V 0.2 N-/RS*), as shown in Fig. 4. A plastic bar was used as a lever to transfer the force generated by the coil and magnet to the load cell, and a small weight (about 2.2 g) was placed on the bar in order to provide an initial bias force, $\mathbf{F}_i$, which was necessary to maintain contact between the plastic bar and the load cell. An excitation frequency of 200 Hz was used for these measurements, since the load cell and measurement system were designed for harmonic excitations. At this frequency, the bar dynamics were found to boost the measured force by a factor of 1.1 over the static drive case, so this factor was used to normalize the resulting force measurements.

The coil and magnet were composed of the same materials as those used in the middle-ear experiments (i.e., 46 gauge wire and Sm_2Co_{17} magnet). In consideration for the minimum force necessary to obtain reliable measurements from the load cell (1% of the maximum allowable force of 0.2 N), and due to limitations on how accurately the gap between the coil and the magnet could be specified (g in Fig. 4), a larger magnet size was chosen. The frustum-shaped magnet had a height of 1.5 mm and a diameter ranging from 1.0 to 1.5 mm, and with its stronger magnetic field, it was able to improve the signal to noise ratio of the load cell measurements by increasing the generated forces. The gap between the coil and the magnet was varied between 2 and 9 mm (determined with an accuracy of around ± 0.2 mm), and for each gap size the force was measured using five different coil currents, ranging in magnitude from 50 to 250 mA, to test for linearity and repeatability.

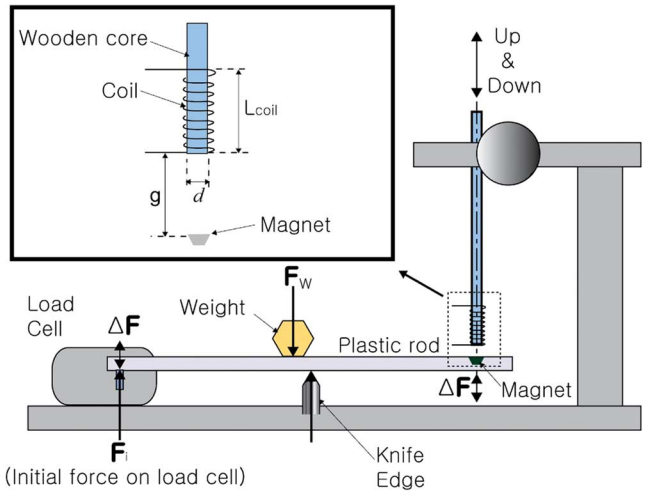

Fig. 4. Force measurement using a load cell in one dimension. The diameter of the wooden core (d) was 6.0 mm, the height of the coil bundle (L_{coil}) was 5.0 mm, the number of coil turns was 50, and the half-length of the plastic bar was 40 mm. The plastic bar was used as a lever to transfer the forces generated by the coil and magnet to the load cell ($\Delta\mathbf{F}$), and the magnitudes of the measured forces were divided by 1.1 to compensate for the effects of bar dynamics at 200 Hz.

E. Work Rate Exerted by Electromagnetic Force

With the middle-ear structures stimulated by the magnet-coil drive system, the magnitude and phase of the velocity at each target were measured using an *OFV 302 LDV* system (*Polytec*) over a frequency range of 0.1–10 kHz. The middle-ear structures were attached to two stacked goniometers, used for changing the incident angle and direction of the laser beam. The goniometer set enabled two orthogonal rotations, with an angular range of $\pm 15^\circ$ about one axis, and $\pm 20^\circ$ about the other axis. Velocities at each target were measured from nine different angular positions of the laser beam, to allow calculation of the 3-D velocity components at each target. Once the 3-D motion components at more than three noncolinear points on the rigid body were defined, the 3-D motion components of the rigid body, consisting of three translations and three rotations, could be calculated from the kinematics of rigid body motion. Fig. 5 shows the magnitudes (left) and phases (right) of the three translational velocities at the tip of the long process of the incus (a) and the three rotational velocities of the incus (b), in the middle-ear experimental setup of Ear 2. See [9] and [10] for detailed procedures for calculation of the 3-D motion components. With the force and moment components and the 3-D motion components of the middle-ear structures, the work rate, P, due to the 3-D

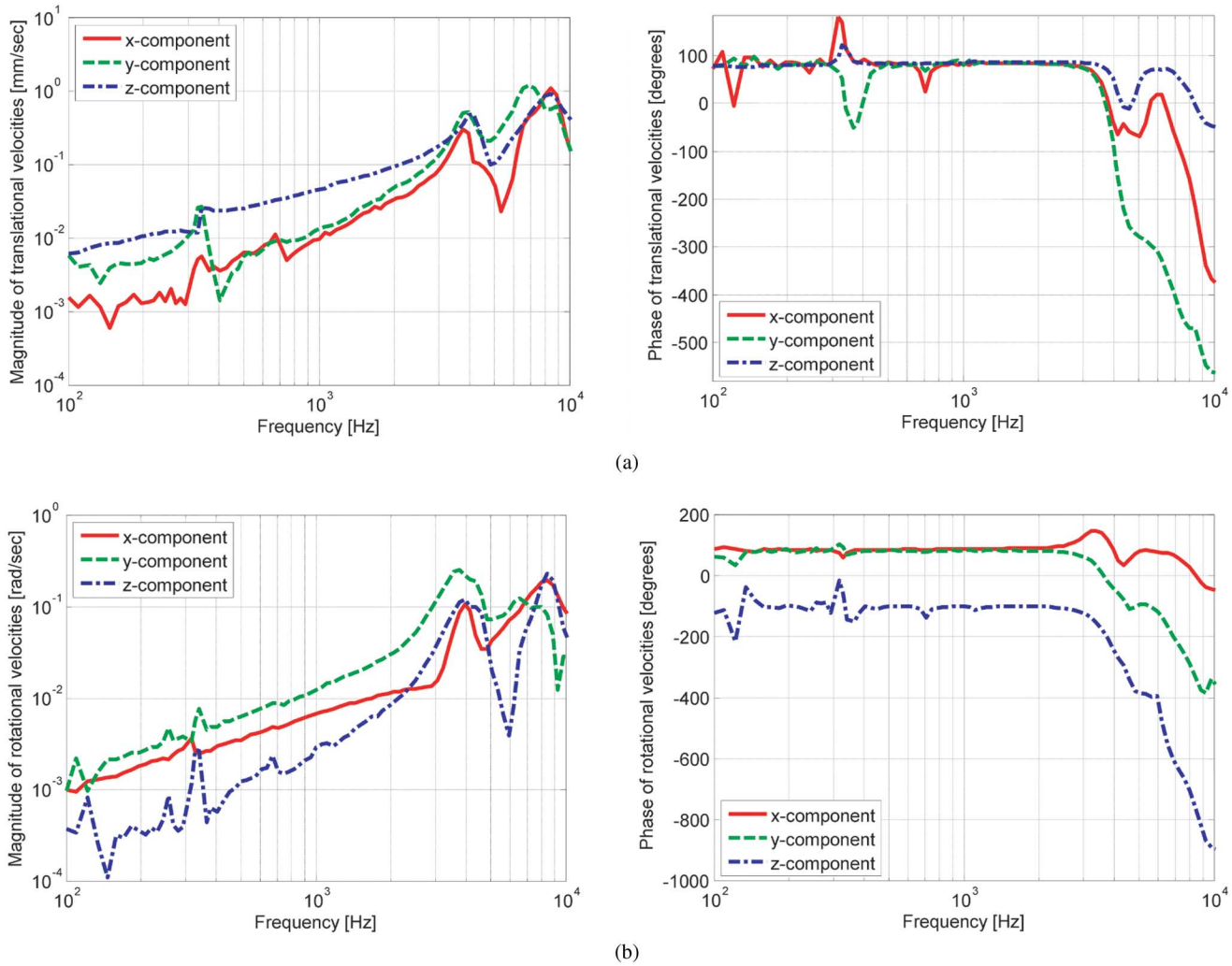

Fig. 5. Measured magnitudes (left) and phases (right) of rigid body motion components with the incus stimulated by the magnet-coil drive system (Ear 2). (a) Three translational velocities at the tip of the long process of the incus, and (b) three rotational velocities of the incus.

force and moment components, is given by the following integral (over one cycle):

$$P = \int_{\text{cycle}} [\text{real}(\mathbf{F}) \cdot \text{real}(\mathbf{v}) + \text{real}(\boldsymbol{\tau}) \cdot \text{real}(\boldsymbol{\omega})]\, dt, \quad (8)$$

where $\mathbf{v}$ and $\boldsymbol{\omega}$ indicate vectors of the translational and rotational velocities at the point upon which the force and moment are acting. Only the real parts of the velocities, force, and moment were used for the work rate calculation. The work rate should be positive, since the force and moment are both applied to a passive middle-ear structure.

III. Results

A. Verification of Force Calculations in One Dimension

The force measurements for each gap were normalized by the coil current, and are plotted in Fig. 6 as circles, while the corresponding calculated values are represented by a sold line. The general agreement among the normalized force measurements causes the overlapping circles to largely appear as a single circle for each gap. The combined noise and artifact levels (plotted as

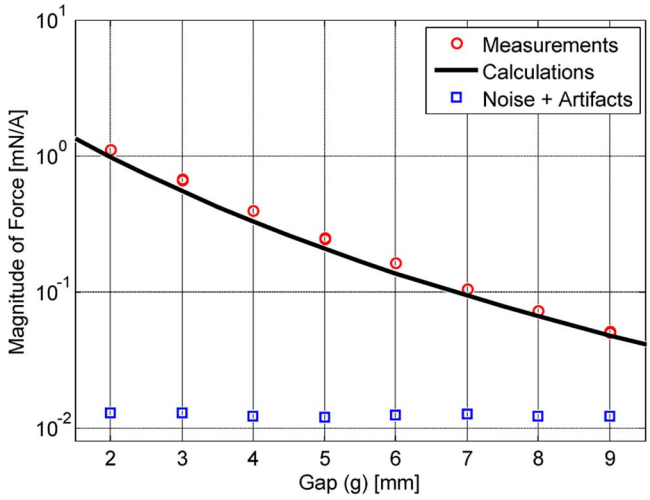

Fig. 6. Comparison of measured forces (circles) and the corresponding calculated forces (solid line) in one dimension. The force measurements at each gap were performed using five different current magnitudes (50–250 mA), at 200 Hz. Each measurement was normalized by the corresponding current magnitude, and at each gap these normalized measurements overlap one another almost completely. The combined noise and artifacts (squares) were measured with a current of 250 mA.

TABLE I
PARAMETERS DESCRIBING THE GEOMETRY OF THE MAGNET AND COIL DRIVE SYSTEM, AS WELL AS CALCULATED FORCES AND MOMENTS ON THE CENTER OF THE MAGNET BASE

	Description	Symbol	Ear 1	Ear 2
Coil Dimensions	Height [mm]	h_c	1.6	1.8
	Inner radius [mm]	Rc_1	4.5	4.6
	Outer radius [mm]	Rc_2	6.1	5.9
	Number of Coil turns	N_c	50	50
Magnet Dimensions	Radius of the face closest to the coil [mm]	Rm_1	0.575	0.575
	Radius of the face farthest from the coil [mm]	Rm_2	0.5	0.5
	Height [mm]	h_m	0.22	0.22
Offsets and Tilt Angles of the Magnet	Offset in the *X* direction [mm]	X_{off}	1.1	0.1
	Offset in the *Y* direction [mm]	Y_{off}	-0.1	-0.2
	Offset in the *Z* direction [mm]	Z_{off}	4.2	8.5
	tilting angle about the *y* axis [degrees]	α	-8	9
	tilting angle about the *z* axis [degrees]	β	-13	58
Forces acting on the Magnet	Component in the *x* direction [μN/A]	F_x	26	-1
	Component in the *y* direction [μN/A]	F_y	-4	-5
	Component in the *z* direction [μN/A]	F_z	-162	-49
Moments acting on the Magnet	Component in the *x* direction [μN·mm/A]	τ_x	-26	-27
	Component in the *y* direction [μN·mm/A]	τ_y	-165	12
	Component in *z* direction [μN·mm/A]	τ_z	2	1

squares) were measured without the magnet in place. The normalized values of the combined noise and artifact were almost constant along the range of currents used in this experiment, and the measurements made with a coil current of 250 mA are plotted in the figure. The measured forces lie well above the noise and artifact levels for all reported gaps.

Most of the error in this measurement can be attributed to the lack of precision in determining the positions of the coil and magnet, as well as to the simplifying assumptions that were made in the calculation procedure. In the context of the middle-ear experimental setup, the relative positions of the coil and magnet were precisely determined from micro-CT images, while in this measurement they were found by referring to a precision scale printed on the wooden core. In modeling the permanent magnet as an equivalent solenoid, the magnetic field intensity vector [$\mathbf{H}$ in (1)] was neglected around the bottom and upper surfaces of the magnet. Errors due to these assumptions become smaller when the magnet is sufficiently tall relative to the diameters of the upper and bottom surfaces. The magnetization vector was also assumed to be homogeneous throughout the whole magnet volume. Differences between the actual coil shape and its simplified torus representation can be another error source. Even given these sources of potential error, the measured forces, with an average error of 13%, are in reasonably close agreement with the calculated values.

B. 3-D Forces and Moments in the Middle-Ear Experiments

Table I contains the *in situ* dimensions and orientations of the magnet and coil drive system, as obtained from the micro-CT scans of the middle-ear preparations. It also contains the magnitudes of the calculated resultant force and moment components (per unit current magnitude) acting upon the center of the bottom surface of the magnet, which is defined as the origin of the magnet frame. See the Methods section for a description of the magnet frame (with its x, y, and z axes) and coil frame (with its X, Y, and Z axes). The magnitude of the force component in the z direction, F_z, is larger for Ear 1 (162 μN/A) than for Ear 2 (49 μN/A) since the magnet is located closer to the coil for Ear 1 ($Z_{\text{off}} = 4.2\ \text{mm}$) than for Ear 2 ($Z_{\text{off}} = 8.5\ \text{mm}$). These force magnitudes would correspond to sound pressure levels (SPL) on the TM of around 80 dB SPL for Ear 1 and 70 dB SPL for Ear 2, given a coil current magnitude of 0.1 A and a TM area of 70 mm^2. The magnitude of the force component in the x direction, F_x, as well as the magnitude of the moment component in the y direction, τ_y, are also larger for Ear 1 due to the closer proximity of the magnet to the ring of the coil in that case.

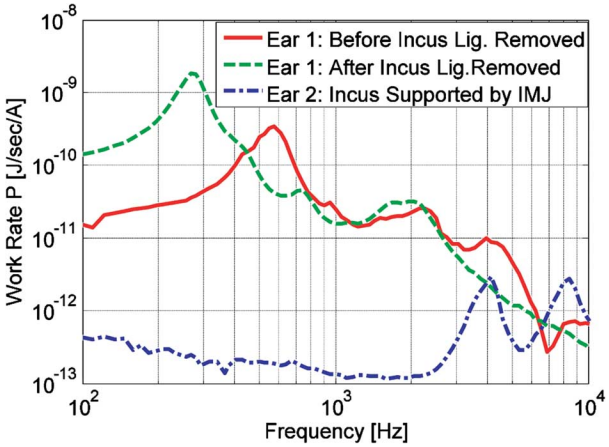

Fig. 7. Work rate exerted by the electromagnetic force. In Ear 1, the work rate was calculated before (solid) and after (dash) the incus ligament was removed. In Ear 2 (dash-dot), the malleus was immobilized using dental cement, and the incus was supported only by the IMJ.

C. Work Rate in the Middle-Ear Experiments

Fig. 7 shows the work rates due to the electromagnetic forces in Ears 1 and 2. As expected, the work rates throughout a cycle showed positive values, for all measured frequencies. The peaks in the work rate curves correspond to resonances of ossicular motions.

In Ear 1, to see the effects of the incus ligament on the vibration of the malleus-incus complex, the 3-D motions of the malleus were measured before and after the incus ligament was removed. Before the incus ligament was removed, the first resonance of the malleus motion occurred around 600 Hz. After the incus ligament was removed, the first resonance was shifted to a lower frequency, around 250 Hz, and the work rate below 400 Hz was increased due to the greater compliance of the structure. From these results, it is presumed that the incus ligament plays a significant role in the MIC motions at low frequencies.

The work rate in Ear 2, where the incus was supported only by the IMJ, showed two clear resonances around 4 and 8.5 kHz, and relatively small work rates below 3 kHz. These results indicate that the relative motion at the IMJ is expected to play a significant role at frequencies above 3 kHz. It was believed for some time that there was no relative motion at the IMJ, and it was recently reported that this joint is deformable at middle frequencies and high frequencies above 3 kHz [17].

D. Control of Force and Moment Components

The forces and moments acting on the magnet (and thus driving the system being studied) can be specified in advance to some degree through the choice of the magnet and coil dimensions and their *in situ* relative positions, as well as by varying the drive current.

Fig. 8(a) shows how the x-component of the calculated force (F_x), acting on the untilted magnet, varies as a function of the magnet position with respect to the coil, X_{off} and Z_{off}, with Y_{off} set to zero. The magnitude of F_x approaches its maximum when the magnet is directly above the center of the ring of the coil $(R_{c1} < X_{\text{off}} < R_{c2})$, and as the magnet gets closer to the coil (i.e., as Z_{off} decreases). The force component in the y direction (F_y, not shown) varies with Y_{off} and Z_{off} (with X_{off} set to zero) in the same manner that F_x varies with X_{off} and Z_{off}, due to symmetry. Fig. 8(b) shows, for the same setup, the positional dependence of the force component in the z direction (F_z). In this case, F_z also increases in magnitude as Z_{off} decreases, but it passes through zero when the magnet is directly above the ring of the coil. F_z reaches its largest positive magnitude when the magnet is positioned directly above the inner radius of the coil $(X_{\text{off}} \approx R_{c1})$, and its largest negative value when it is positioned directly above the outer radius of the coil $(X_{\text{off}} \approx R_{c2})$. Fig. 8(c) shows, also for the same setup, how the moment component in the y direction (τ_y) depends on X_{off} and Z_{off}. Similarly to F_x, the magnitude of τ_y becomes larger both as Z_{off} decreases and as X_{off} approaches the point directly above the ring of the coil. The dependence of the moment component along the x direction (τ_x, not shown) on Y_{off} and Z_{off} is the same as the dependence of τ_y on X_{off} and Z_{off}, due to symmetry. The moment component in the z direction (τ_z) has a relatively small magnitude when the magnet is untilted.

Fig. 8(d) shows how F_x and F_z are affected when the magnet is tilted about the y axis by an angle α, for the case of $X_{\text{off}} = Y_{\text{off}} = 0$ mm, $Z_{\text{off}} = 4$ mm, and $\beta = 0°$. F_x is zero when α is zero, since $X_{\text{off}} = 0$ mm, but F_x increases to its maximum value when α reaches 90°. Conversely, F_z has its maximum value when α is zero, and decreases to zero when α reaches 90°. When the α angle is 90°, τ_y (not shown) also reaches its maximum value for the given magnet position.

IV. Discussion

The accuracy of the force and the moment calculations is limited in part by the accuracy with which one can measure the dimensions, relative positions, and orientations of the magnet and coil. The micro-CT imaging modality presently allows *in situ* measurements of the dimensions and orientations of the magnet and coil with resolutions on the order of 10 μm, but this degree of accuracy requires that the entire specimen be able to fit inside the 38.5-mm diameter scan space. Current *in vivo* CT imaging techniques appropriate for larger structures are limited to resolutions on the order of 125 μm [18]. As the distance between the coil and the magnet becomes smaller, the proportion of error in the position measurements becomes more significant. For example, if the distance between a coil element and a magnet element were 5 mm, which is close to the case for Ear 1, then an error of one pixel in determining the positions from the scans would cause an error of 5%–8% in the resulting magnetic field calculation with a 125 μm scan resolution, but only 0.4%–0.6% with a 10.5 μm scan resolution (see (5)). If the initial distance between the two elements were 2 mm, however, then a single pixel error in measuring the distance would cause an error in the resulting magnetic field calculation of 14%–21% with a 125 μm resolution, but only 1.1%–1.6% with a 10.5 μm resolution. As the resolution of *in vivo* imaging becomes higher, the accuracy and convenience of the noncontact force calculation methods proposed here will improve.

Other sources of error include simplifications that were made in the calculations, and nonuniformity in the magnetization of the magnet (see Section II). The shape of the actual coil bundle was not exactly the same as the simplified shape used in the calculations, and by modeling the permanent magnet as an equivalent solenoid, the magnetic field intensity factor was neglected around the bottom and upper surfaces of the magnet.

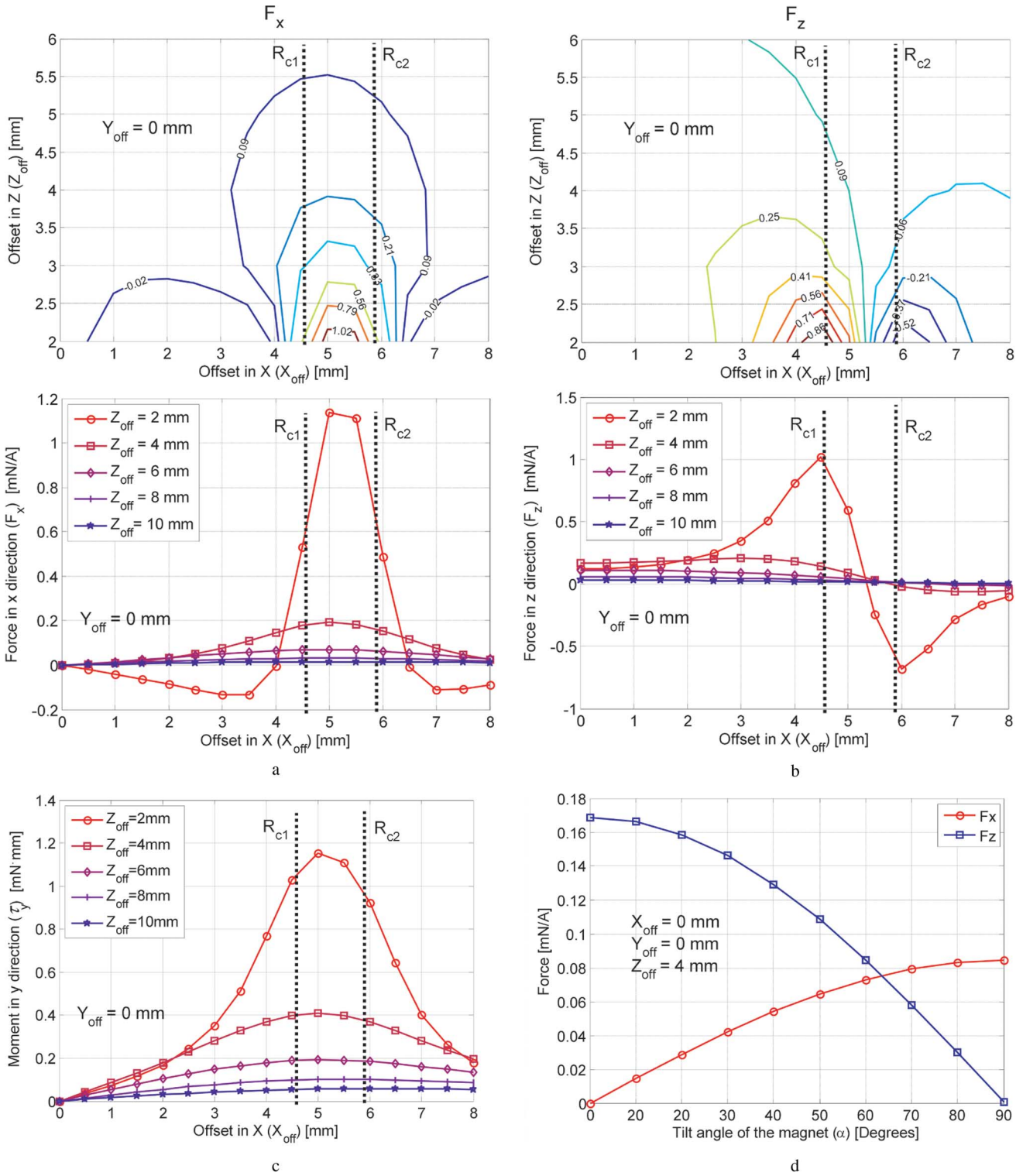

Fig. 8. Calculated forces and moments acting on the magnet as functions of the magnet position and tilt angle. (a) Two depictions of the force component in the x direction (F_x), as a function of the X and Z offsets of the magnet, (b) two depictions of the force component in the z direction (F_z), as a function of the X and Z offsets of the magnet, (c) moment component in the y direction (τ_y), as a function of the X and Z offsets of the magnet, and (d) the effects of tilting the magnet about the y axis on F_x and F_z, as a function of tilt angle α. Magnet tilt angles were set to zero for (a), (b), and (c), and for (d) the tilt angle about the z axis (β) was set to zero. The magnet offsets for (d) were fixed at $X_{\text{off}} = 0$ mm, $Y_{\text{off}} = 0$ mm, and $Z_{\text{off}} = 4$ mm.

The magnet was also assumed to have a uniform magnetization per unit volume, though the datasheet from the manufacturer indicates that the magnetization can vary within a $\pm 3\%$ range throughout the magnet volume. However, even with such errors, this method of calculating forces and moments still provides a useful way of realistically estimating the directions and magnitudes of the 3-D drive forces and moments.

The force components in the xy plane are maximized when the untilted magnet is located directly above the ring of the coil, while the magnitude of the force component in the z direction

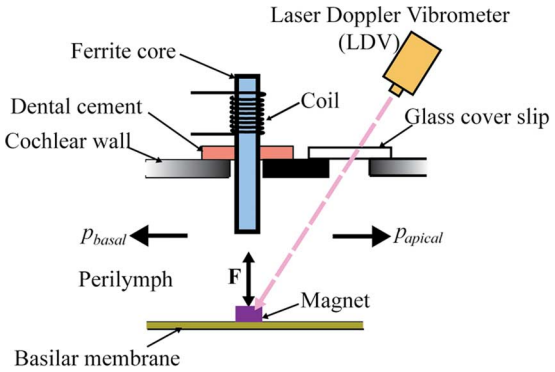

Fig. 9. An application of the magnet and coil drive system to the excitation of the basilar membrane and fluid spaces within the cochlea. The magnitude of the force can be specified by choosing the distance between the magnet and the ferrite core, the number of turns in the coil, and the amount of current flowing in the coil. The force acting on the magnet is used to generate an apical pressure (p_{apical}) wave and a basal pressure (p_{basal}) wave. The basal pressure wave would then travel through the middle ear, and could be measured in the ear canal as an otoacoustic emission.

passes through zero in this position. Additional flexibility in specifying the forces and moments acting on the magnet could conceivably be achieved using an array of coil bundles and independently controlling the magnitude and phase of the current in each of the coils.

In this study, the magnet-coil force motor was used to stimulate the isolated structures in the mammalian middle ear, which was done in the context of a study that aimed to characterize the dynamics of the entire middle ear. The calculated work rates showed characteristics of the isolated middle-ear structures. Such measurements using calculated and controlled stimulation can also be used to find mechanical properties of the middle-ear supporting structures.

Another application of this force motor method is for the study of how otoacoustic emissions travel outward from the cochlea to the stapes and ear canal. A small magnet (∼0.1 mg) would be placed on the basilar membrane inside the cochlea, and a coil wrapped around a ferromagnetic core would then be used to drive the magnet (Fig. 9). The force acting on the basilar membrane due to the interaction between the magnet and the coil would then generate pressure waves in the fluid of the cochlea that would produce stapes footplate motion (measurable using Laser Doppler Vibrometry), as well as pressure in the ear canal (measurable using a probe tube microphone) [19].

ACKNOWLEDGMENT

The authors wish to thank J. Fay and J. Winstead for providing the force measurement setup, as well as Prof. R. White, K. N. O'Connor, and J. Fay for valuable comments.

REFERENCES

[1] K. Autumn *et al.*, "Evidence for van der Waals adhesion in gecko setae," *Proc. Natl. Acad. Sci.*, vol. 99, pp. 12252–12256, 2002.
[2] T. Dumon, O. Zennaro, J. M. Aran, and J. P. Bebear, "Piezoelectric middle ear implant preserving the ossicular chain," *Otolaryngol Clin. North Amer.*, vol. 8, no. 1, pp. 173–187, 1995.
[3] S. M. Tanaka, "New mechanical stimulator for cultured cone cells using piezoelectric actuator," *J. Biomechanics*, vol. 32, pp. 427–430, 1999.
[4] P. K. Plinkert *et al.*, "In-vivo experiments in the cat with an implantable piezoelectric hearing aid transducer," *Eur. Arch. Otorhinolaryngol*, vol. 257, pp. 304–313, 2000.
[5] B. Masterton, H. Heffner, and R. Ravizza, "The evolution of human hearing," *J. Acoust. Soc. Amer.*, vol. 45, no. 4, pp. 966–985, 1969.
[6] E. H. Colbert and M. Morales, "Evolution of the vertebrates," in *A History of the Backboned Animals Through Time*. New York: Wiley, 1991.
[7] G. Fleischer, "Evolutionary principles of the mammalian middle ear," *Advances in Anatomy Embryology and Cell Biology*, vol. 55, pp. 3–70, 1978, Fasc. 5.
[8] H. E. Heffner and R. S. Heffner, "High-frequency hearing," in *The Senses: A comprehensive reference*. San Diego, CA: Academic, 2008, vol. 3, pp. 55–60.
[9] W. F. Decraemer, S. M. Khanna, and W. R. J. Funnel, "A method for determining three-dimensional vibration in the ear," *Hearing Research*, vol. 77, pp. 19–37, 1994.
[10] J. H. Sim, "Imaging, physiology, and biomechanics of the malleus-incus complex," Ph.D. dissertation, Stanford Univ., Stanford, CA, 2007.
[11] G. Wang, D. L. Snyder, J. A. O'Sullivan, and M. W. Vannier, "Iterative deblurring for CT metal artifact reduction," *IEEE Trans. Med. Imaging*, vol. 15, pp. 657–664, 1996.
[12] G. Wang and M. W. Vannier, "Metal artifacts," in *Computerized Tomography in Encyclopedia of Electrical and Electronics Engineering*. New York: Wiley, 1998.
[13] J. H. Sim, S. Puria, and C. R. Steele, "Calculation of inertia properties of the malleus-incus complex using micro-CT imaging," *J. Mech. Mater. Struct.*, vol. 2, no. 8, pp. 1515–1524, 2007.
[14] J. H. Sim and S. Puria, "Soft Tissue morphometry of the malleus-incus complex from micro-CT imaging," *J. Assoc. Res. Otolaryngology*, vol. 9, pp. 5–21, 2008.
[15] M. A. Plonus, "H and B field for permanent magnet-equivalent-current formulation," in *Applied Electromagnetics*. New York: McGraw-Hill, 1988.
[16] J. van Bladel, "Stationary magnetic fields," in *Electromagnetic fields*. Bristol, PA: Hemisphere, 1985.
[17] U. B. Willi, M. A. Ferrazzini, and A. M. Huber, "The incudo-malleolar joint and sound transmission losses," *Hearing Research*, vol. 174, pp. 32–44, 2002.
[18] N. Yanagihara, S. Nakamura, H. Furutaguchi, T. Hinohira, and K. Yamada, "Measurement of normal middle ear using xyz slice view tomography," presented at the 3rd Symp. Middle Ear Mechanics in Research and Otology, Matsuyama, Ehime, Japan, Jul. 9–12, 2003.
[19] S. Puria, K. N. O'Connor, H. Yamada, Y. Shimizu, G. Popelka, and C. R. Steele, "Do otoacoustic emissions travel in the cochlea via slow or fast waves?," presented at the 32nd ARO Middle Winter Meeting, Baltimore, MD, Feb. 14–19, 2009.

Jae Hoon Sim received B.S. and M.A. degrees from Seoul National University, Seoul, Korea, and the Ph.D. degree from Stanford University, Stanford, CA, with a topic of middle-ear mechanics.

He worked as a Research Engineer and Assistant at the Institute of Advanced Design and Machining Center, Seoul National University, the MEMS Department of Daewoo Electronics, and the Veterans Affairs Palo Alto Heath Care System. He is currently the Head of the Middle-Ear Research Laboratory at the ORL-Klinik of UniversitätsSpital Zürich. His research interests include micro-CT imaging and dynamics of the middle and inner-ear structures.

Sunil Puria received the B.E.E.E. degree from the City College of New York in 1983, the M.S. degree from Columbia University, New York, in 1985, and the Ph.D. degree from the City University of New York in 1991. He did most of his Ph.D. thesis work at AT&T Bell Labs, Murray Hills, NJ.

He then went on to do a Postdoctoral Fellowship at the Massachusetts Institute of Technology (MIT), Cambridge, and was an Adjunct Faculty Member at Harvard University Medical School until 1997. Currently, he is an Engineer-Scientist, holding dual positions at Stanford University as an Associate Professor (Consulting) in the Departments of Mechanical Engineering and Otolaryngology-HNS, and as the Chief Scientist at EarLens Corporation. He has published nearly 40 papers in peer-reviewed journals, and has seven issued patents. Most recently, he was the Chair of the Middle-Ear Mechanics in Research in Otology (MEMRO) 2009 International meeting at Stanford University. His areas of specialty are biomechanics, physiology, imaging of the auditory system, and novel hearing aid technologies.